Generic Source Parameter Determination and Ground-Motion Prediction for Earthquake Early Warning

Itzhak Lior*[1] and Alon Ziv[1]

ABSTRACT

Currently available earthquake early warning systems employ region-specific empirical relations for magnitude determination and ground-motion prediction. Consequently, the setting up of such systems requires lengthy calibration and parameter tuning. This situation is most problematic in low seismicity and/or poorly instrumented regions, where the data available for inferring those empirical relations are scarce. To address this issue, a generic approach for real-time magnitude, stress drop, and ground-motion prediction is introduced that is based on the omega-squared model. This approach leads to the following approximate expressions for seismic moment: $M_0 \propto RT^{0.5}D_{rms}^{1.5}/V_{rms}^{0.5}$, and stress drop: $\Delta\tau \propto RT^{0.5}A_{rms}^{3}/V_{rms}^{2}$, in which R is the hypocentral distance; T is the data interval; and D_{rms}, V_{rms}, and A_{rms} are the displacement, velocity, and acceleration root mean squares, respectively, which may be calculated in the time domain. The potential of these relations for early warning applications is demonstrated using a large composite data set that includes the two 2019 Ridgecrest earthquakes. A quality parameter is introduced that identifies inconsistent earthquake magnitude and stress-drop estimates. Once initial estimates of the seismic moment and stress drop become available, the peak ground velocity and acceleration may be estimated in real time using the generic ground-motion prediction equation of Lior and Ziv (2018). The use of stress drop for ground-motion prediction is shown to be critical for strong ground accelerations. The main advantages of the generic approach with respect to the empirical approach are that it is readily implementable in any seismic region, allows for the easy update of magnitude, stress drop, and shaking intensity with time, and uses source parameter determination and peak ground motion predictions that are subject to the same model assumptions, thus constituting a self-consistent early warning method.

KEY POINTS

- A generic approach for real-time source parameter determination and ground motion prediction is presented.
- The approach is evolutionary, region independent, and uses self-consistent source and ground motion prediction.
- This method is advantageous in regions where the data available for implementing empirical methods are scarce.

Supplemental Material

INTRODUCTION

Reliably predicting ground-shaking intensity in real time is a key for regional earthquake early warning systems (EEWS). Operational EEWS currently in use accomplish this task in three consecutive steps as follows: (1) detection and epicenter location, (2) magnitude determination, and (3) ground-motion prediction (e.g., Allen, 2007; Hoshiba and Ozaki, 2014; Zollo *et al.*, 2014; Nof and Allen, 2016; Colombelli and Zollo, 2016; Festa *et al.*, 2018; Given *et al.*, 2018). Because in practice, steps 2–3 employ region-specific empirical relations, the setting up of new EEWS may require a lengthy system calibration phase, especially in places where earthquake rate is low and/or the instrumental data available for establishing such empirical relations are insufficient. To date, the preferred approach for addressing the problem of limited data sets is to generate synthetic data via stochastic finite-fault simulations for a selection of earthquake scenarios (e.g., Pittore *et al.*, 2014). Yet, replacing the region-specific relations with generic ones, which are readily implementable in any tectonic environment, holds

1. Department of Geosciences, Tel-Aviv University, Tel-Aviv, Israel

*Corresponding author: itzhaklior22@gmail.com

Cite this article as Lior, I., and A. Ziv (2020). Generic Source Parameter Determination and Ground-Motion Prediction for Earthquake Early Warning, *Bull. Seismol. Soc. Am.* **110**, 345–356, doi: 10.1785/0120190140

much promise for expediting the setting of new EEWS and circumvents the necessity for stochastic modeling. In this study, we introduce a generic approach for source parameter determination and ground-motion prediction that builds on the theoretical relations between ground shaking and source parameters described in Lior and Ziv (2018; hereafter, LZ18).

According to fault models, the far-field displacement spectra of body waves are flat below the corner frequency and are decaying asymptotically to f^{-n} above it, with n that is equal to 2 or 3 ($n = 2$: Aki, 1967; Brune, 1970; Sato and Hirasawa; 1973; Madariaga, 1976; $n = 3$: Haskell, 1964, 1966; Kostrov, 1964; Dahlen, 1974; Boatwright, 1980). The exponent n is determined by the highest order discontinuity in the displacement pulse (Bracewell, 1965), which in turn depends on the model assumptions. Some researchers attribute this discontinuity to the slip onset, and some to the rupture arrest. Brune (1970) showed that $n = 2$ results from a displacement pulse that is initially linear. In contrast, Savage (1972) argued that the initial rise in the displacement pulse with time should be quadratic, resulting in $n = 3$. Sato and Hirasawa (1973) showed that the f^{-2} decay is produced by the stopping phase resulting from the abrupt rupture arrest, and Boatwright (1980) demonstrated that an f^{-3} amplitude fall-off may result from rupture arrest that is preceded by a phase of decelerating rupture growth. Often, however, real data cannot discriminate between the different models. Thanks to its simplicity and the generally good agreement with far-field records of small-to-moderate magnitudes, Brune's omega-squared hypothesis is the most commonly used for determining fault dimensions.

With this background, in this study we adopt the omega-squared model of Brune (1970), describing the far-field body waves spectra as

$$\frac{d^m}{dt^m}\Omega(f) = (2\pi f)^m \frac{\Omega_0}{1 + (\frac{f}{f_0})^2}, \tag{1}$$

in which Ω_0 and f_0 are the two source-related spectral parameters, f is the frequency, and $m = 0$, 1, or 2 are for displacement, velocity, or acceleration spectra, respectively. At distances relevant to EEWS, anelastic attenuation is of little importance (Wu and Zhao, 2006; Van Houtte *et al.*, 2011; Lior *et al.*, 2016), and the attenuation is attributed primarily to the effect of subsurface geological structure near the site. Following Anderson and Hough (1984), the effect of the near-site attenuation may be described by a decaying exponent: $\exp(-\pi\kappa_0 f)$, with κ_0 being a site-specific frequency-independent attenuation parameter (for a complete review of κ taxonomy, we refer the reader to Ktenidou *et al.*, 2014). Thus, the far-field attenuated source spectra is modeled as

$$\frac{d^n}{dt^n}\Omega(f) = (2\pi f)^n \frac{\Omega_0}{1 + (\frac{f}{f_0})^2} \exp(-\pi\kappa_0 f). \tag{2}$$

Using equation (2), LZ18 obtained a set of exact expressions for displacement, velocity, and acceleration root mean squares (rms) that may be approximated as

$$D_{\mathrm{rms}} = \Omega_0 \sqrt{\frac{\pi}{2T}\frac{f_0}{1 + 0.5\pi^2\kappa_0 f_0}}, \tag{3a}$$

$$V_{\mathrm{rms}} = 2\pi\Omega_0 \sqrt{\frac{\pi}{2T}\left(\frac{f_0}{1 + \pi^{4/3}\kappa_0 f_0}\right)^3}, \tag{3b}$$

and

$$A_{\mathrm{rms}} = (2\pi)^2\Omega_0 \frac{f_0^2}{\sqrt{\pi\kappa_0 T}(1 + 1.5^{-1/4}\pi\kappa_0 f_0)^2}, \tag{3c}$$

with T being the data interval. The data interval adopted in this study is that used by Lior and Ziv (2017):

$$\mathrm{T} = 1/f_0 + R/C_s, \tag{4}$$

in which R is the hypocentral distance and C_S is the S wave velocity. The first term accounts for the rupture duration (Hanks and McGuire, 1981), and the second approximately corrects for the stretching of the waveforms with increasing distance. The spectral parameters Ω_0 and f_0 are related to the seismic moment M_0 and stress drop $\Delta\tau$ as

$$M_0 = \frac{\Omega_0 4\pi\rho C^3 R}{U_{\varphi\theta} F_s}, \tag{5a}$$

and

$$\Delta\tau = \frac{7}{16} M_0 \left(\frac{f_0}{kC_S}\right)^3, \tag{5b}$$

in which $U_{\varphi\theta}$ is the radiation pattern, F_s is the free-surface correction factor, ρ is the density, k is a constant assigned with a different value for P and S waves (Sato and Hirasawa, 1973; Madariaga, 1976), and C stands for the wave velocity, with C_P and C_S for P and S waves, respectively. Combining equations (3a), (3b), (3c)–(5a), (5b), with the relations between rms and peak motions (equations 19 in LZ18) yields a set of ground-motion prediction equations (GMPEs):

$$\mathrm{PGD} = 2.1 M_0^{5/6} \Delta\tau^{1/6} \frac{\beta_D}{R\sqrt{\frac{1}{kC_S}(\frac{7}{16}\frac{M_0}{\Delta\tau})^{1/3} + R/C_S}[1 + 0.5\pi^2\kappa_0 kC_S(\frac{16}{7}\frac{\Delta\tau}{M_0})^{1/3}]^{1/2}}, \tag{6a}$$

$$\mathrm{PGV} = 2.9\sqrt{M_0\Delta\tau}\,\frac{\beta_V}{R\sqrt{\frac{1}{kC_S}\left(\frac{7}{16}\frac{M_0}{\Delta\tau}\right)^{1/3} + R/C_S\left[1+\pi^{4/3}\kappa_0 kC_S\left(\frac{16}{7}\frac{\Delta\tau}{M_0}\right)^{1/3}\right]^{3/2}}}, \quad (6b)$$

and

$$\mathrm{PGA} = 3.3M_0^{1/3}\Delta\tau^{2/3}\,\frac{\beta_A}{R\sqrt{\kappa_0\left[\frac{1}{kC_S}\left(\frac{7}{16}\frac{M_0}{\Delta\tau}\right)^{1/3} + R/C_S\right]\left[1+1.5^{-1/4}\pi\kappa_0 kC_S\left(\frac{16}{7}\frac{\Delta\tau}{M_0}\right)^{1/3}\right]^2}}, \quad (6c)$$

for peak ground displacement (PGD), peak ground velocity (PGV), and peak ground acceleration (PGA), in which $\beta_D = U_{\varphi\theta}F_s(16/7)^{1/6}\sqrt{kC_S}/(\sqrt{2\pi}4\rho C_S^3)$, $\beta_V = 2\pi U_{\phi\theta}Fs\sqrt{16/7}(kC_S)^{3/2}/(\sqrt{2\pi}4\rho C_S^3)$, and $\beta_A = 4\pi U_{\phi\theta}Fs(16/7)^{2/3}(kC_S)^2/(\sqrt{\pi}4\rho C_S^3)$ (equations 20 in LZ18). A plot of PGA as a function of magnitude for stress drops of 1 and 10 MPa is presented in Figure 1, which shows that the peak motion caused by large magnitude earthquakes is strongly stress drop dependent. This highlights the importance of determining not only the earthquake magnitude, but also its stress drop (Ziv and Lior, 2016). In a later part of this article, we show that equations (6a), (6b), and (6c) perform well without any prior knowledge of site and path conditions, as other empirical methods require. However, if enough such prior knowledge is available, these effects may be accounted for through site-specific and path-dependent attenuation and/or amplitude corrections. Next, simple expressions for seismic moment and stress drop are derived. Then, the potential of these new expressions and the GMPE for earthquake early warning (EEW) is examined using a composite catalog.

EXPRESSIONS FOR SEISMIC MOMENT AND STRESS DROP

As demonstrated by Lior and Ziv (2017, 2018), the product of κ_0 and f_0 is a fundamental parameter in describing the spectral shape, and, therefore, also the earthquake size. The attenuation parameter varies little (Lior and Ziv, 2018), whereas the corner frequency, which is inversely proportional to the rupture radius (e.g., Brune, 1970; Madariaga, 1976), varies over several orders of magnitude. From linear regression of many data sets, the corner frequency and the seismic moment are related through $M_0 \propto f_0^p$ with p between −3 and −4 (e.g., Archuleta *et al.*, 1982; Gibowicz *et al.*, 1991; Abercrombie, 1995; Gusev *et al.*, 2002; Hiramatsu *et al.*, 2002). Thus, very large $\kappa_0 f_0$ corresponds to small earthquakes, and vice versa. Asymptotic analysis of equations (3a), (3b), and (3c) with respect to $\kappa_0 f_0$ yields distinct expressions for large and small earthquakes. The large earthquake solutions are (Hanks, 1979; McGuire and Hanks, 1980; Luco, 1985; Lior *et al.*, 2016; Lior and Ziv, 2017, 2018):

$$\lim_{\kappa f_0\to 0} D_{\mathrm{rms}} = \Omega_0\sqrt{\frac{\pi}{2T}f_0}, \quad (7a)$$

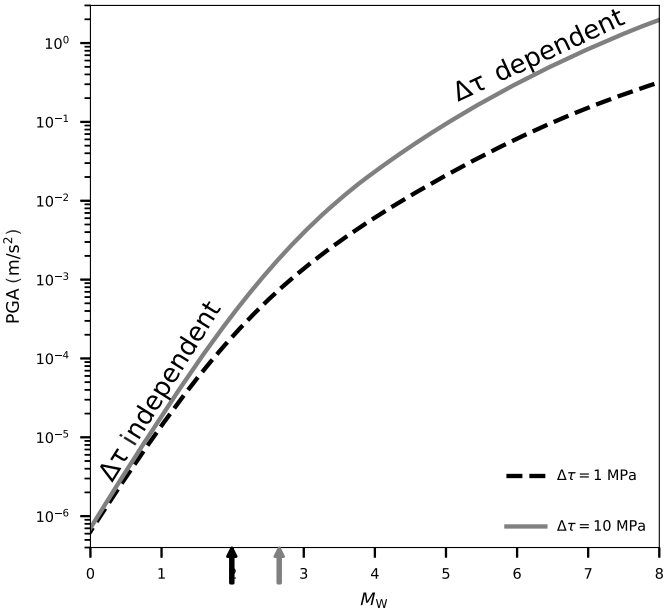

Figure 1. Peak ground acceleration (PGA) as a function of magnitude for stress drops of 1 and 10 MPa (equation 6c). Arrows indicate the transition between the stress-drop dependent and independent regimes.

$$\lim_{\kappa f_0\to 0} V_{\mathrm{rms}} = 2\pi\Omega_0\sqrt{\frac{\pi}{2T}f_0^3}, \quad (7b)$$

$$\lim_{\kappa f_0\to 0} A_{\mathrm{rms}} = (2\pi)^2\Omega_0\frac{f_0^2}{\sqrt{\pi\kappa_0 T}}, \quad (7c)$$

and the small ones are (Luco, 1985; Lior and Ziv, 2017, 2018):

$$\lim_{\kappa f_0\to\infty} D_{\mathrm{rms}} = \Omega_0\sqrt{\frac{1}{\pi\kappa_0 T}}, \quad (8a)$$

$$\lim_{\kappa f_0\to\infty} V_{\mathrm{rms}} = 2\pi\Omega_0\sqrt{\frac{1}{2(\pi\kappa_0)^3 T}}, \quad (8b)$$

$$\lim_{\kappa f_0\to\infty} A_{\mathrm{rms}} = (2\pi)^2\Omega_0\sqrt{\frac{1}{\sqrt{2/3}(\pi\kappa_0)^5 T}}. \quad (8c)$$

The ground shaking caused by large earthquakes depends on both Ω_0 and f_0, whereas that caused by smaller quakes depends only on Ω_0. The transition between the two regimes corresponds to the transition between the $\Delta\tau$-dependent and $\Delta\tau$-independent regimes in Figure 1. From equations (7a), (7b), and (7c), Ω_0 and f_0 may be expressed as

$$\Omega_0 = 2\sqrt{T}\frac{D_{\mathrm{rms}}^{1.5}}{\sqrt{V_{\mathrm{rms}}}}, \tag{9a}$$

$$f_0 = \frac{1}{4}\sqrt{\frac{\kappa_0}{\pi}}\frac{A_{\mathrm{rms}}}{\sqrt{V_{\mathrm{rms}}D_{\mathrm{rms}}}}. \tag{9b}$$

Similarly, from equations (8a), (8a), and (8c) Ω_0 may be written as

$$\Omega_0 = \sqrt{\sqrt{2}\pi}\sqrt{T}\frac{D_{\mathrm{rms}}^{1.5}}{\sqrt{V_{\mathrm{rms}}}} \approx 2.1\sqrt{T}\frac{D_{\mathrm{rms}}^{1.5}}{\sqrt{V_{\mathrm{rms}}}}. \tag{10}$$

Inspection of the asymptotic solutions reveals nearly identical expressions for Ω_0 of small and large earthquakes. Thanks to the similarity between equations (9a) and (10), and the insensitivity of the GMPEs in equations (6a), (6b), and (6c) to the stress drop of small earthquakes (Fig. 1), use of the large earthquake approximations in equations (9a) and (9b) should work, regardless of earthquake magnitude. Thus, in this study the approximate expressions in equations (9a) and (9b) are employed for the entire magnitude range.

Finally, combining equations (5a), (5b) and (9a), (9b), the seismic moment and stress drop may be expressed in terms of the ground motion rms as follows:

$$M_0 = C_M R T^{0.5}\frac{D_{\mathrm{rms}}^{1.5}}{V_{\mathrm{rms}}^{0.5}}, \tag{11a}$$

$$\Delta\tau = C_{\Delta\tau} R T^{0.5}\frac{A_{\mathrm{rms}}^{3}}{V_{\mathrm{rms}}^{2}}, \tag{11b}$$

in which C_M and $C_{\Delta\tau}$ collect all the source and medium constants and are equal to:

$$C_M = \frac{8\pi\rho C^3}{U_{\phi\theta}F_s}, \tag{12a}$$

$$C_{\Delta\tau} = \frac{7\rho C^3\kappa_0^{1.5}}{128\pi^{0.5}U_{\varphi\theta}F(kC_S)^3}. \tag{12b}$$

As is the case for standard source parameter calculations, use of the aforementioned expressions yields more stable and more trustable results for the seismic moment than for the stress drop (Cotton *et al.*, 2013; Lior and Ziv, 2018). Our experience shows that when the data interval is shorter than the rupture duration, the stress-drop expression may return unphysical results corresponding to corner frequencies smaller than $1/T$. To ensure physically sound combinations of seismic moment and stress drop, we require f_0 to be larger than $1/T$:

$$\Delta\tau = \max\left(\frac{7}{16}C_M R T^{0.5}\frac{D_{\mathrm{rms}}^{1.5}}{V_{\mathrm{rms}}^{0.5}}(TkC_S)^{-3}, C_{\Delta\tau}RT^{0.5}\frac{A_{\mathrm{rms}}^{3}}{V_{\mathrm{rms}}^{2}}\right). \tag{13}$$

Because the rms of the ground motion may be calculated directly from the seismogram in the time domain, the implementation of equations (11a) and (13) in real time is rather straightforward. Once these parameters are known, they may be plugged in the GMPE (equations 6a, 6b, and 6c) to map the predicted peak shaking. Equations (6a), (6b), (6c) and (11a), (11b) are generic in the sense that they are readily implementable in any tectonic environment, without having to go through a calibration and tuning phase.

POTENTIAL FOR EEW

The potential of the new source parameter expressions and the GMPE for EEWS is examined using the part of the composite catalog complied by Lior and Ziv (2017), for which reliable source parameter estimates were obtained by LZ18. To this data, we added records of the 2019 M_w 6.4 and 7.1 Ridgecrest earthquakes. The new dataset includes a total of 5957 three-component seismograms, of which 3008 were recorded by California Integrated Seismic Network (2701 velocity and 307 acceleration records), and 2894 were recorded by Japan's K-NET and KiK-net surface accelerometers. The remaining 55 seismograms are associated with the 2010 M_w 7.2 Baja California earthquake and the 1999 M_w 7.6 Chi-Chi earthquake and were extracted from the Pacific Earthquake Engineering Research–Next Generation Attenuation of Ground Motions (PEER NGA) database (Ancheta *et al.*, 2014). The total number of earthquakes is 625, of which 462 are from California and 161 are from Japan. Their magnitudes range between 3 and 7.6, and their hypocentral distances are limited to 100 km (Fig. 2 and Figs. S1–S4, available in the supplemental material to this article). Small magnitudes ($M_w < 4$) are included to demonstrate that false alarms do not occur using the proposed method. All records were manually reviewed and picked. Displacement, velocity, and acceleration time series were obtained by integration or differentiation, followed by high-pass filtering at 0.01 Hz. The rms of the ground displacement, velocity, and acceleration were calculated in the time domain according to $\mathrm{sqrt}[\sum_{i=1}^{l}(Z_i^2 + E_i^2 + N_i^2)/l]$, in which Z, E, and N are the ground-motion amplitudes in the vertical, east, and north directions, respectively, and l is the number of samples. The parameter setting used throughout this study is detailed in Table 1.

Seismic moment and stress drop

The real-time seismic moment and stress-drop calculator is called, once a first estimate of epicenter location becomes available. This requirement implies waiting for four *P*-phase picks as in Satriano *et al.* (2008) or two *P*-phase picks integrated with one or two back azimuths, as in Eisermann *et al.* (2015). In this study, R is calculated from the catalog location. At each triggered station, seismic moment and stress drops are calculated

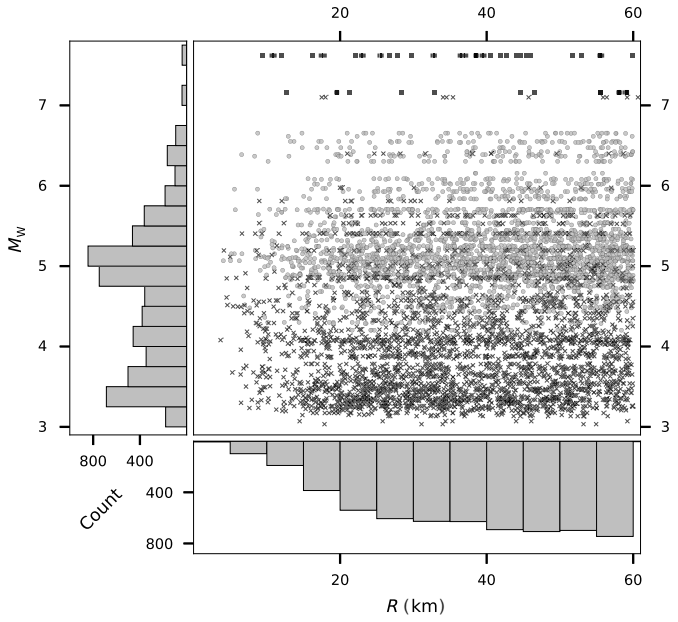

Figure 2. Data distribution according to moment magnitude and distance, with the former calculated according to Lior and Ziv (2018) and the latter taken from the local catalogs. × symbols and circles indicate data from California and Japan, respectively, and squares indicate records of the M_w 7.6 Chi-Chi and the M_w 7.2 Baja California earthquakes.

for increasing data intervals using equations (11a) and (13), respectively. For data intervals larger than about $R/8$ (here R is in kilometers), the P and S phases get mixed up. Because these equations contain phase-specific constants ($U_{\varphi\theta}$, C, and k), it is sensible to weight average those coefficients according to the fraction of each phase. Thus, the S–P interval is approximated using $T_{S-P} = R/8$, and the phase-dependent coefficients are obtained using (Ziv and Lior, 2016):

$$\text{const} = \frac{T_{S-P}}{T}\text{const}_P + \frac{T - T_{S-P}}{T}\text{const}_S, \tag{14}$$

in which const stands for $C^3/U_{\varphi\theta}$ or k^3.

The agreement between real-time and catalog source parameters are assessed, with the latter calculated according to LZ18. Exceptions are the five largest earthquakes, whose catalog moment magnitudes are the ones reported by the U.S. Geological Survey National Earthquake Information Center. Real-time seismogram-specific M_w estimates as a function of the catalog M_w are shown in Figure 3 for 2, 4, and 6 s long data intervals. Upon increasing the data interval, the scatter in the real-time magnitude decreases, and the agreement with the catalog M_w improves. The improvement in the magnitude estimates with increased data intervals is expected for large earthquakes, because their rupture durations are longer than those of smaller ones. Because our approach is model based, the consistency between model predictions and actual observations may be quantified, and inconsistent data may be either downweighted or disregarded. Specifically, our generic approach rests completely on the premise that at each seismic station, and for every point in time, the observed ground motions are well described by the Brune's predicted GMPEs in equations (3a), (3b), and (3c). To quantify the discrepancy between Brune's predicted and observed motion, an inconsistency index is introduced:

$$\text{Inconsistency index} = \max\left(\left|\log\left(\frac{A_{\text{rms}}^{\text{obs}}}{A_{\text{rms}}^{\text{cal}}}\right)\right|, \left|\log\left(\frac{V_{\text{rms}}^{\text{obs}}}{V_{\text{rms}}^{\text{cal}}}\right)\right|, \left|\log\left(\frac{D_{\text{rms}}^{\text{obs}}}{D_{\text{rms}}^{\text{cal}}}\right)\right|\right), \tag{15}$$

in which the superscripts obs and cal stand for observed and calculated ground-motion rms, respectively. Observed ground-motion rms are calculated directly from the time series, whereas calculated rms are obtained using equations (3a), (3b), and (3c) with parameters Ω_0 and f_0 estimated via equations (9a) and (9b) for the available data interval. As expected, results with large inconsistency index (red symbols) are more scattered and plot further away from the 1:1 line than those with small inconsistency index (green symbols). Event-average magnitude and stress-drop estimates (× symbols in Figs. 3 and

TABLE 1
Parameter Setting

Parameter	Reference	First Appears
$\kappa = 0.025$ s	Lior and Ziv (2018)	Equation (2)
$\rho = 2600$ km/m^3		Equation (5a)
$C : C_P = 5333$ m/s (P wave), $C_S = 3200$ m/s (S wave)		Equation (5a)
$U_{\phi\theta} : U_{\phi\theta} = 0.52$ (P wave), $U_{\phi\theta} = 0.63$ (S wave)	Aki and Richards (1980)	Equation (5a)
$F_S = 2$	Aki and Richards (1980)	Equation (5a)
$k : k = 0.32$ (P wave), $k = 0.21$ (S wave)	Madariaga (1976)	Equation (5b)
$\beta : \beta_D = 4.39 \times 10^{-14}$ m$^{0.5}$ s$^{2.5}$/kg, $\beta_V = 2.44 \times 10^{-10}$ m$^{1.5}$s$^{1.5}$/kg, $\beta_A = 2.05 \times 10^{-18}$ m^{2}s/kg	Calculated using Madariaga (1976) k	Equations (6a), (6b), (6c)
$C_M : C_M = 9.52 \times 10^{15}$ kg/s^3 (P wave), $C_M = 1.7 \times 10^{15}$ kg/s^3 (S wave)		Equation (11a)
$C_{\Delta\tau} : C_{\Delta\tau} = 43.1$ s$^{1.5}$kg/m^3 (P wave), $C_{\Delta\tau} = 27.2$ s$^{1.5}$kg/m^3 (S wave)		Equation (11b)

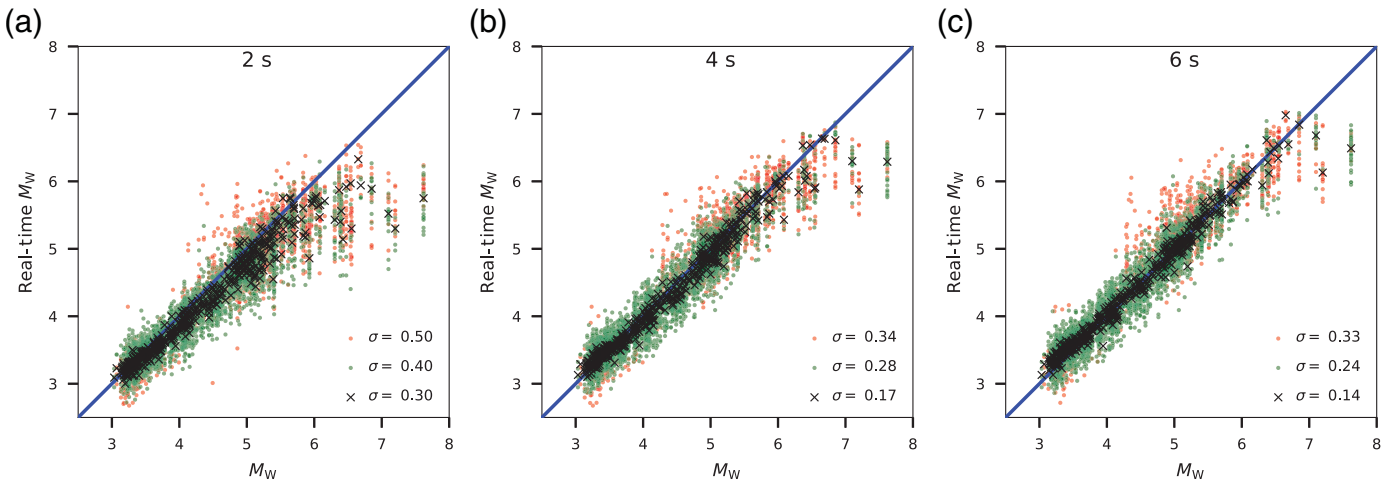

Figure 3. Real-time magnitude as a function of catalog magnitudes for different data intervals starting at the time of first *P*-phase arrival. (a) Result for 2 s long interval. (b) Result for 4 s long interval. (c) Result for 6 s long interval. Single-seismogram estimates, whose inconsistency indices are smaller and larger than 0.35 are indicated by green and red symbols, respectively, and event averages are indicated by × symbols. Standard deviations of the magnitude discrepancies are indicated at the bottom-right corner of each panel. The blue line is a 1:1 line.

4), weight averaged by the inverse of the inconsistency index, exhibit good agreement with catalog values compared with that of an empirical method (see the Comparison with an empirical approach section). Real-time $\Delta\tau$ estimates are compared to catalog $\Delta\tau$ in Figure 4. Previous studies predict that single station f_0 estimates may vary by a factor of 1.5–2 (Sato and Hirasawa, 1973; Madariaga, 1976; Dong and Papageorgiou, 2002; Kaneko and Shearer, 2015; Ross and Ben-Zion, 2016), which translates to a factor of ∼3.5–8 of $\Delta\tau$ variability [0.5–0.9 in $\log(\Delta\tau)$]. That the standard deviation of the $\log(\Delta\tau)$ discrepancies (reported at the bottom-right corner of Fig. 4) is of similar magnitude to that reported by previous studies suggests an overall satisfactory agreement between real-time and actual $\Delta\tau$. That agreement improves gradually with increasing data interval, which allows better assessment of the lower frequency content (not shown).

Optimal performance for EEWS applications is achieved by integrating the source parameter calculator into an evolutionary algorithm. The results of such an evolutionary approach are shown in Figure 5 for four large earthquakes. In these examples, seismogram-specific magnitudes were updated repeatedly for increasing data intervals, starting at the time of the first *P*-phase pick and ending when the ground-motion rms (acceleration or velocity) reaches its maximum value or the total data interval reaches 60 s, whichever occurs first. The solid bold lines indicate event-average estimates, weight averaged by the available interval and by the inverse of the inconsistency index. The results for the two Honshu earthquakes, with M_w of 6.7 and 6.8, are extremely stable, and are indicating the right magnitude (i.e., within half a magnitude unit) from the very first output, after about 4 s of the first trigger. In contrast, initial estimates of the M_w 7.2 Baja California earthquake are more than a magnitude unit below the catalog value. Event average value of this earthquake is reaching half a magnitude unit of the catalog magnitude after 30 s of the origin. Finally, the magnitude of the M_w 7.6 Chi-Chi earthquake is more severely underestimated, with a final estimate that is 0.4 magnitude unit below the catalog magnitude. The somewhat poorer result for the Chi-Chi earthquake is not

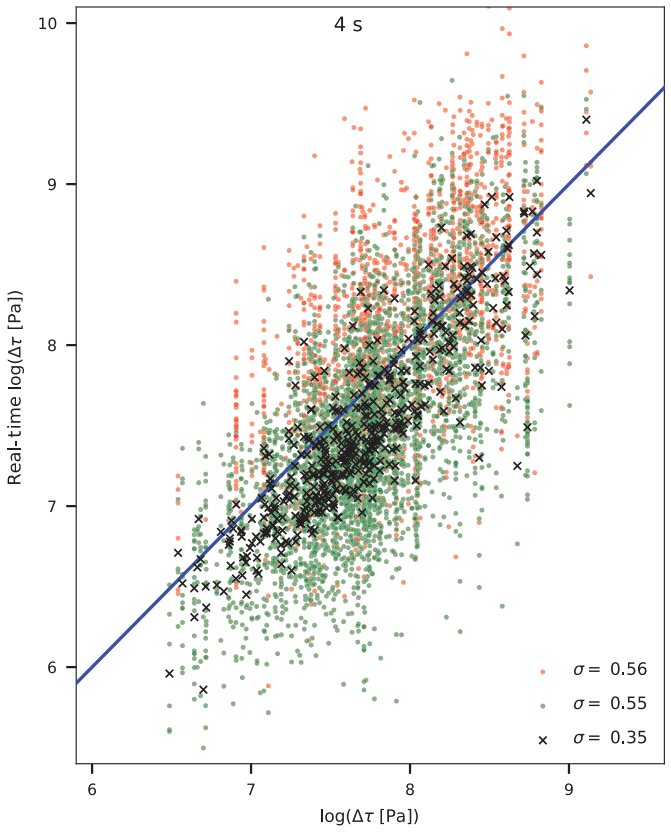

Figure 4. Real-time stress drop calculated with $T = 4$ s as a function of catalog stress drop. Symbols and color code are as in Figure 3. Standard deviations of the stress-drop discrepancies are reported at the bottom-right corner. The blue curve is a 1:1 line.

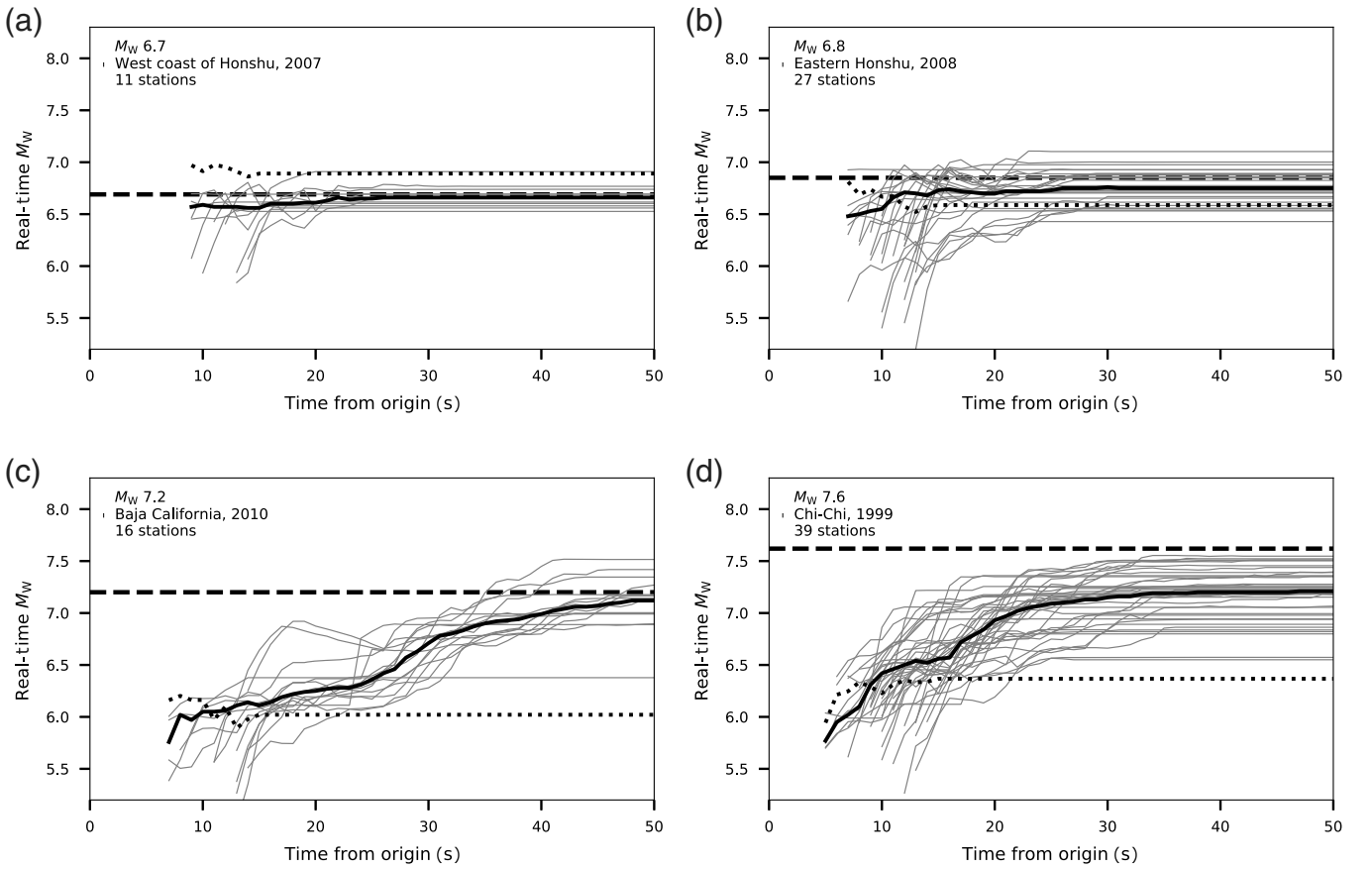

Figure 5. Evolutionary magnitude estimates as a function of time since the origin time, for the (a) 25 March 2007 M_w 6.7 west of Honshu, (b) 14 June 2008 M_w 6.8 eastern Honshu, (c) 4 April 2010 M_w 7.2 Baja California, and (d) 21 September 1999 M_w 7.6 Chi-Chi earthquakes. Thin gray and thick black lines indicate single-station estimates and event averages, respectively. Dotted line indicates event-averaged empirically based magnitude employing the magnitude–distance–peak displacement (Pd) relation of Kuyuk and Allen (2013). Horizontal dashed line indicates catalog magnitude.

surprising, given that this earthquake is known to have initially radiated very weak ground motions (e.g., Ma *et al.*, 2001; Wang *et al.*, 2002; Lee *et al.*, 2007).

Ground-motion prediction

Prerequisites for ground-motion prediction are earthquake location, magnitude, and stress drop. Once initial estimates of these parameters become available, the PGV and PGA may be estimated in real time using the GMPE of LZ18 (equations 6a, 6b, 6c). Unlike empirical GMPEs implemented in regional EEWS (e.g., Boore and Atkinson, 2008) that are functions of magnitude and hypocentral distance, the GMPE of LZ18 also accounts for the stress drop, thus providing better constraint on peak ground motions (Fig. 1). The discrepancies between real-time predicted and observed PGV and PGA are shown in Figure 6 as a function of distance using 4 s long data intervals for $M_w < 7$ and 30 s long data intervals for $M_w > 7$. The distributions of these discrepancies for different magnitude bins are also shown. In general, the agreement between predicted and observed ground motions is neither a function of distance nor a function of magnitude, suggesting both parameters are properly modeled by the GMPE.

DISCUSSION

Below, the merit of the generic approach is further assessed in light of the July 2019 M_w 6.4 and 7.1 Ridgecrest earthquakes, and in reference to an empirical magnitude relation.

The 2019 Ridgecrest earthquakes example

Real-time generic magnitude estimates of the July 2019 M_w 6.4 and 7.1 Ridgecrest earthquakes are shown in Figure 7 (solid curves) as a function of time. For the M_w 6.4 earthquake, these estimates are stable and are close to the catalog magnitude from the very start (as in Fig. 5a,b). In contrast, magnitude estimates of the M_w 7.1 earthquake are initially more than one magnitude unit below the catalog magnitude (as in Fig. 5c,d), jumping to M_w of 6.5 after 10 s from the origin and to 7 about 20 s later. The agreement between the modified Mercalli intensity (Worden *et al.*, 2012) and predicted and observed peak ground motion is examined in Figure 8. Ten seconds from the origin time, both PGV and PGA are underpredicted. Because of its greater sensitivity to magnitude (equations 6a, 6b, 6c), PGV is more underpredicted than PGA (Fig. 8a,b). The magnitude estimate improves with increasing time since the origin time (Fig. 7), and consequently also the underprediction of peak ground motion diminishes (Fig. 8c,d). At the same time, the predicted

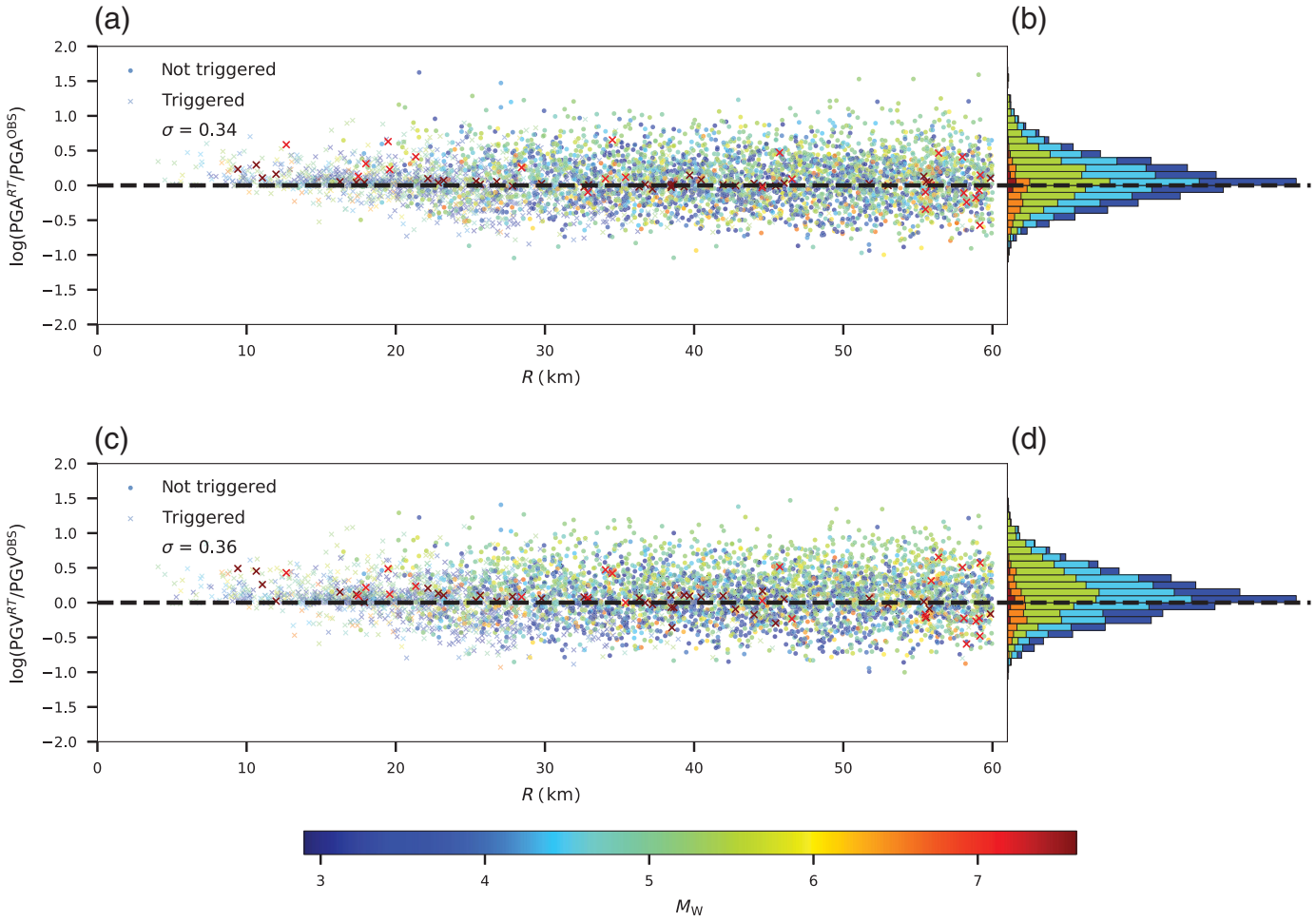

Figure 6. Discrepancies between predicted and observed peak ground motions as a function of distance and magnitude. (a) PGA discrepancies as a function of distance. (b) Histogram of PGA discrepancies for different magnitude bins. (c) Peak ground velocity (PGV) discrepancies as a function of distance. (d) Histogram of PGV discrepancies for different magnitude bins. Predicted ground motions, PGA^{RT} and PGV^{RT}, are obtained using equation (6a), (6b), and (6c), with real-time magnitudes and stress drops calculated with $T = 4$ s for $M_w < 7$ and $T = 30$ s for $M_w > 7$. Circles and × symbols indicate not-yet-triggered and already-triggered stations, respectively. Peak motion discrepancies are reported at the top-left corner of each panel. Color code corresponds to the catalog magnitudes.

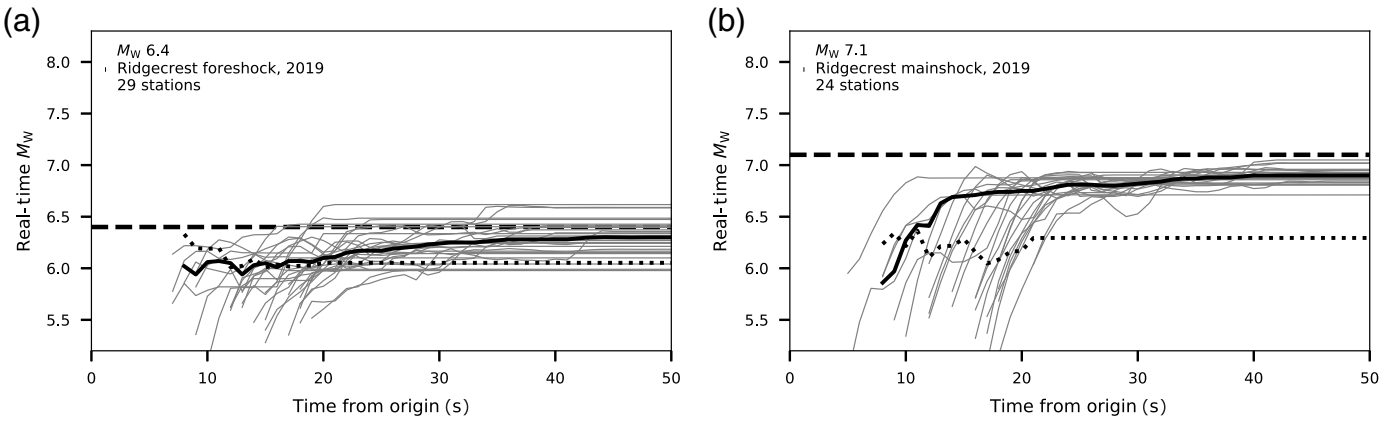

Figure 7. Evolutionary magnitude estimates as a function of time from origin, for the (a) 4 July 2019 Ridgecrest M_w 6.4, (b) 5 July 2019 Ridgecrest M_w 7.1 earthquakes. Thin gray and thick black lines indicate single-station estimates and event averages, respectively. Dotted line indicates event-averaged empirically based magnitude employing the magnitude–distance–Pd relation of Kuyuk and Allen (2013). Horizontal dashed line indicates catalog magnitude.

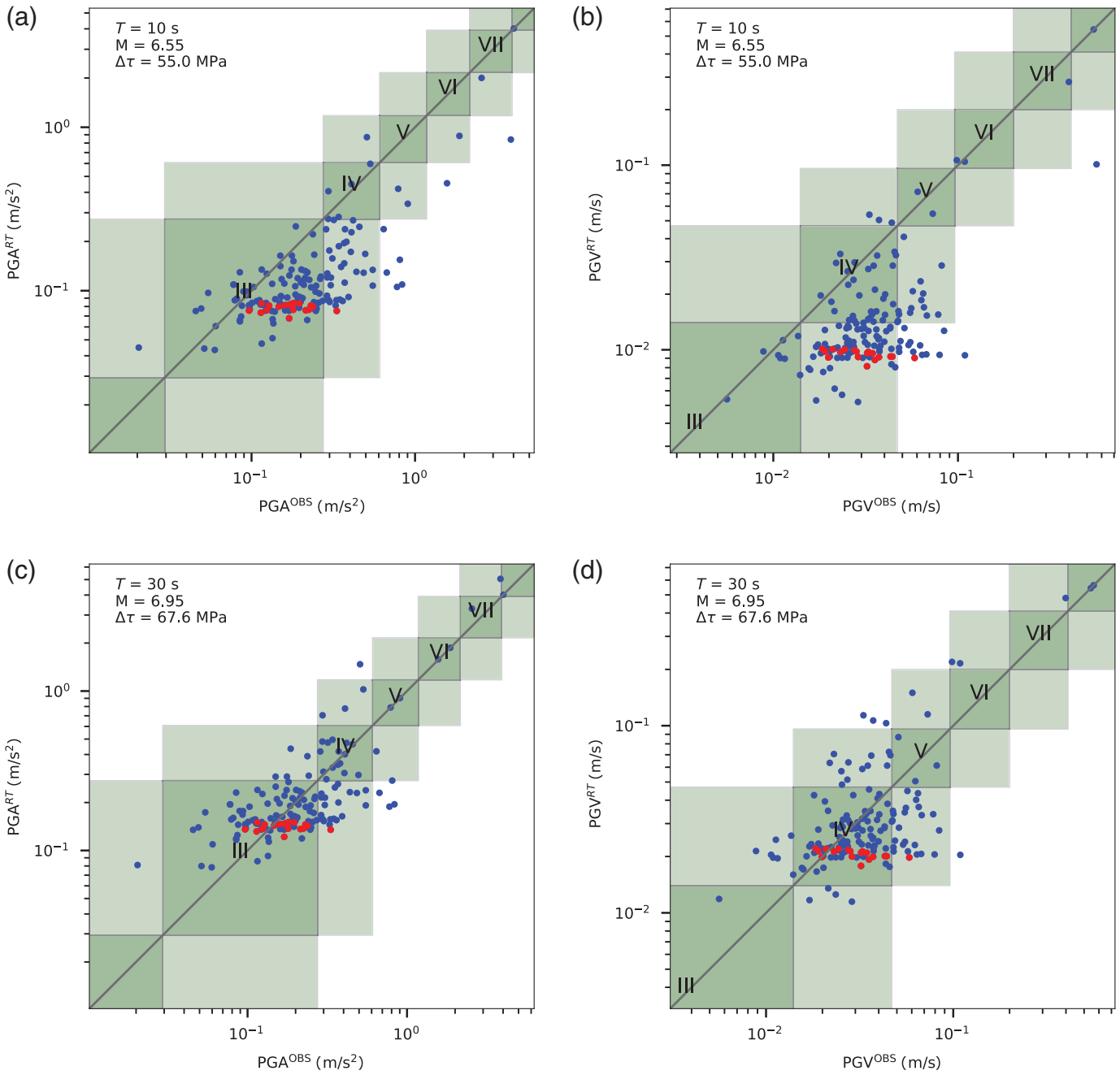

Figure 8. Predicted versus observed peak ground motions and Mercalli intensities for the M_w 7.1 Ridgecrest earthquake. Predicted PGA as a function of observed PGA for (a) 10 and (c) 30 s from origin. Predicted PGV as a function of observed PGV for (b) 10 and (d) 30 s from origin. Intensity levels are indicated by green rectangles, a one unit difference indicated by light green rectangles. Data recorded at Los Angeles are marked in red.

intensity for Los Angeles (red symbols) equals four using the intensity-PGV relation of Worden *et al.* (2012), in agreement with "Did You Feel It?" reports. The improvement of magnitude estimates with time of $M_w > 7$ earthquakes highlights the merit of the evolutionary approach.

Comparison with an empirical approach

A common approach for determining earthquake magnitude in real time is to use empirical equations that relate the catalog magnitude with hypocentral distance and peak ground motion (displacement or velocity) during a short interval starting at the time of the *P*-phase arrival. Numerous such empirical relations are reported in the literature. Here, the Kuyuk and Allen (2013) relation is chosen for comparison with the generic magnitude approach. That relation has been established for 4 s long data intervals using data from Japan and California and is currently implemented by the California EEWS (Kohler *et al.*, 2017). In implementing that empirical magnitude relation, we adhered to the same data processing methodology currently implemented by the California EEWS (Kuyuk and Allen, 2013, and references therein). Catalog and station-specific empirically

based magnitude estimates are compared in Figure S5. Following the practice in California EEWS, and to facilitate the comparison with Figure 3, intervals of 2 and 4 s are used. The scatter of the empirically based magnitudes with respect to the 1:1 line is twice larger than that of the generic approach (Fig. 3). It is thus concluded that the empirically based approach is significantly more prone to false and missed alarms than the generic approach introduced in this study. EEWS that adopt empirical relations do not implement evolutionary magnitude calculation of more than few seconds. Consequently, the magnitudes of $M_w > 7$ earthquakes are severely underestimated (dotted curves in Figs. 5 and 7). That single-station magnitude estimates increase with time (thin gray curves in Figs. 5 and 7) clearly demonstrates the advantage of extending the analysis past the initial 4 s.

SUMMARY

Commonly used schemes for real-time magnitude determination and ground-motion prediction employ empirical magnitude–distance–amplitude relations. In addition to these relations being region specific, and therefore may not apply globally, the quality of their prediction is limited by the quality and quantity of the available seismic record. The latter issue is especially critical in regions of low-seismic rate and/or limited instrumental record.

A new approach was introduced in this study that uses the model-based (Brune, 1970; Anderson and Hough, 1984) results of LZ18. This approach led to simple expressions for the seismic moment and stress drop (equations 11a, 11b). The potential of these expressions and the GMPEs of LZ18 were examined using $\kappa_0 = 0.025$ s. Despite the use of constant κ_0, good agreement is found between calculated and observed EEW parameters for a dataset sampling diverse tectonic settings and site conditions. The merit of the new approach was further demonstrated with respect to the July 2019 M_w 6.4 and 7.1 Ridgecrest earthquakes, and in reference to the empirical magnitude relation of Kuyuk and Allen (2013). Thus, it is concluded that the new approach is generic and performs well without prior knowledge of the site conditions. Nevertheless, in places where site-specific κ_0 are available, plugging them into these equations may enhance their performances.

The model-based approach presents three main advantages with respect to the empirical approach. First, it may be implemented in any seismic region, thus addressing the data availability issue. Second, its integration into an evolutionary algorithm, in which magnitude, stress drop, and ground-motion prediction are updated with increasing data intervals, is straightforward. Third, unlike EEWS that implement source parameter schemes and GMPEs were derived separately, here, they are subject to the same model assumptions, and thus constitute a self-consistent EEW method. Occasionally, hypocentral distances may be comparable to the rupture length. In such cases, Brune's far-field model is not valid. Currently, there is no theoretical formulation describing ground motions in the near field. If and when such formulation becomes available, it may be used to improve results for near-field records.

DATA AND RESOURCES

The data used in this study were obtained from the Southern California Earthquake Data Center (Caltech dataset, http://scedc.caltech.edu/, last accessed May 2019), the K-NET and KiK-net strong-motion networks (http://www.kyoshin.bosai.go.jp/, last accessed January 2016) and from the Pacific Earthquake Engineering Research (PEER) ground-motion database (http://ngawest2.berkeley.edu/site/, last accessed January 2016). The supplemental material contains earthquake location maps and a comparison between catalog and station-specific magnitude estimates using an empirical magnitude–distance–amplitude relation.

ACKNOWLEDGMENTS

The authors thank Associate Editor Stefano Parolai and two anonymous reviewers for their constructive remarks. The authors also thank Ran Nof for discussions surrounding Figure 7. This research was supported by Grant Number 1081/14 from the Israel Science Foundation.

REFERENCES

Abercrombie, R. E. (1995). Earthquake source scaling relationships from −1 to 5 M_L using seismograms recorded at 2.5-km depth, *J. Geophys. Res.* **100,** 24,015–24,036, doi: 10.1029/95JB02397.

Aki, K. (1967). Scaling law of seismic spectrum, *J. Geophys. Res.* **72,** no. 4, 1217–1231.

Aki, K., and P. G. Richards (1980). *Quantitative Seismology: Theory and Methods*, W. H. Freeman, San Francisco, California.

Allen, R. M. (2007). The ElarmS earthquake early warning methodology and application across California, in *Earthquake Early Warning Systems*, P. Gasparini, G. Manfredi, and J. Zschau (Editors), Springer-Verlag, Heidelberg, Berlin, Germany, doi: 10.1007/978-3-540-72241-0_3.

Ancheta, T. D., R. B. Darragh, J. P. Stewart, E. Seyhan, W. J. Silva, B. S. J. Chiou, K. E. Wooddell, R. W. Graves, A. R. Kottke, D. M. Boore, *et al.* (2014). NGA-West2 database, *Earthq. Spectra* **30,** 989–1005, doi: 10.1193/070913EQS197M.

Anderson, J. G., and S. E. Hough (1984). A model for the shape of the Fourier amplitude spectrum of acceleration at high frequencies, *Bull. Seismol. Soc. Am.* **74,** 1969–1993.

Archuleta, R. J., E. Cranswick, C. Mueller, and P. Spudich (1982). Source parameters of the 1980 Mammoth Lakes, California, earthquake sequence, *J. Geophys. Res.* **87,** 4595–4607.

Boatwright, J. (1980). A spectral theory for circular seismic sources; simple estimates of source dimension, dynamic stress drop, and radiated seismic energy, *Bull. Seismol. Soc. Am.* **70,** no. 1, 1–27.

Boore, D., and G. Atkinson (2008). Ground-motion prediction equations for the average horizontal component of PGA, PGV, and 5%-damped PSA at spectral periods between 0.01 s and 10.0 s, *Earthq. Spectra* **24,** 99–138, doi: 10.1193/1.2830434.

Bracewell, R. N. (1965). *The Fourier Transform and Its Applications*, McGraw-Hill Book Company, New York, New York.

Brune, J. N. (1970). Tectonic stress and the spectra of seismic shear waves from earthquakes, *J. Geophys. Res.* **75,** 4997–5009, doi: 10.1029/JB075i026p04997.

Colombelli, S., and A. Zollo (2016). Rapid and reliable seismic source characterization in earthquake early warning systems: Current methodologies, results, and new perspectives, *J. Seismol.* **20,** 1171–1186, doi: 10.1007/s10950-016-9570-z.

Cotton, F., R. Archuleta, and M. Causse (2013). What is sigma of the stress drop?, *Seismol. Res. Lett.* **84,** 42–48, doi: 10.1785/0220120087.

Dahlen, F. A. (1974). On the ratio of P-wave to S-wave corner frequencies for shallow earthquake sources, *Bull. Seismol. Soc. Am.* **64,** 1159–1180.

Dong, G., and A. S. Papageorgiou (2002). Seismic radiation from a unidirectional asymmetrical circular crack model, Part II: Variable rupture velocity, *Bull. Seismol. Soc. Am.* **92,** 962–982, doi: 10.1785/0120010209.

Eisermann, A. S., A. Ziv, and G. H. Wust-Bloch (2015). Real-time back azimuth for earthquake early warning, *Bull. Seismol. Soc. Am.* **105,** 2274–2285, doi: 10.1785/0120140298.

Festa, G., M. Picozzi, A. Caruso, S. Colombelli, M. Cattaneo, L. Chiaraluce, L. Elia, C. Martino, S. Marzorati, M. Supino, and A. Zollo (2018). Performance of earthquake early warning systems during the 2016–2017 Mw 5–6.5 Central Italy sequence, *Seismol. Res. Lett.* **89,** 1–12.

Gibowicz, S. J., R. P. Young, S. Talebi, and D. J. Rawlence (1991). Source parameters of seismic events at the underground research laboratory in Manitoba Canada: Scaling relations for events with moment magnitude smaller than -2, *Bull. Seismol. Soc. Am.* **81,** 1157–1182.

Given, D. D., R. M. Allen, A. S. Baltay, P. Bodin, E. S. Cochran, K. Creager, L. Gee, E. Hauksson, T. H. Heaton, M. Hellweg, *et al.* (2018). Revised technical implementation plan for the Shakealert system–An earthquake early warning system for the West Coast of the United States, *U.S. Geol. Surv. Open-File Rept. 2018-1155*, 42 pp., doi: 10.3133/ofr20181155.

Gusev, A., M. Radulian, M. Rizescu, and G. F. Panza (2002). Source scaling of intermediate-depth Vrancea earthquakes, *Geophys. J. Int.* **151,** 879–889.

Hanks, T. C. (1979). b values and $\omega^{-\gamma}$ seismic source models: Implications for tectonic stress variations along active crustal fault zones and the estimation of high-frequency strong ground motion, *J. Geophys. Res.* **84,** 2235–2241, doi: 10.1029/JB084iB05p02235.

Hanks, T. C., and R. K. McGuire (1981). The character of high-frequency strong ground motion, *Bull. Seismol. Soc. Am.* **71,** 2071–2095.

Haskell, N. A. (1964). Total energy and energy spectral density of elastic wave radiation from propagating faults, *Bull. Seismol. Soc. Am.* **54,** 1811–1841.

Haskell, N. A. (1966). Total energy and energy spectral density of elastic wave radiation from propagating faults, Part II. A statistical source model, *Bull. Seismol. Soc. Am.* **56,** 125–140.

Hiramatsu, Y., H. Yamanaka, K. Tadokoro, K. Nishigami, and S. Ohmi (2002). Scaling law between corner frequency and seismic moment of microearthquakes: Is the breakdown of the cube law a nature of earthquakes?, *Geophys. Res. Lett.* **29,** 1211, doi: 10.1029/2001GL013894.

Hoshiba, M., and T. Ozaki (2014). Earthquake early warning and tsunami warning of the Japan meteorological agency, and their performance in the 2011 off the Pacific Coast of Tohoku earthquake (Mw 9.0), in *Early Warning for Geological Disasters: Scientific Methods and Current Practice*, F. Wenzel and J. Zschau (Editors), Springer-Verlag, Heidelberg, Berlin, Germany, doi: 10.1007/978-3-642-12233-0_1.

Kaneko, Y., and P. M. Shearer (2015). Variability of seismic source spectra, estimated stress drop, and radiated energy, derived from cohesive-zone models of symmetrical and asymmetrical circular and elliptical ruptures, *J. Geophys. Res.* **120,** 1053–1079, doi: 10.1002/2014JB011642.

Kohler, M. D., E. S. Cochran, D. Given, S. Guiwits, D. Neuhauser, I. Henson, R. Hartog, P. Bodin, V. Kress, S. Thompson, *et al.* (2017). Earthquake early warning ShakeAlert system: West coast wide production prototype, *Seismol. Res. Lett.* **89,** no. 1, 99–107, doi: 10.1785/0220170140.

Kostrov, B. V. (1964). Self-similar problems of propagation of shear cracks, *J. Appl. Math. Mech.* **28,** 1077–1087.

Ktenidou, O.-J., F. Cotton, N. Abrahamson, and J. G. Anderson (2014). Taxonomy of κ: A review of definitions and estimation approaches targeted to applications, *Seismol. Res. Lett.* **85,** 135–146, doi: 10.1785/0220130027.

Kuyuk, S. H., and R. M. Allen (2013). A global approach to provide magnitude estimates for earthquake early warning alerts, *Geophys. Res. Lett.* **40,** no. 24, 6329–6333, doi: 10.1002/2013GL058580.

Luco, J. (1985). On strong ground motion estimates based on models of the radiated spectrum, *Bull. Seismol. Soc. Am.* **75,** 641–649.

Lee, S., H. Chen, and K. Ma (2007). Strong ground motion simulation of the 1999 Chi-Chi, Taiwan earthquake from a realistic three-dimensional source and crustal structure, *J. Geophys. Res.* **112,** no. B06307, doi: 10.1029/2006JB004615.

Lior, I., and A. Ziv (2017). The relation between ground acceleration and earthquake source parameters: Theory and observations, *Bull. Seismol. Soc. Am.* **107,** 1012–1018, doi: 10.1785/0120160251.

Lior, I., and A. Ziv (2018). The relation between ground motion, earthquake source parameters and attenuation: Implications for source parameter inversion and ground motion prediction equations, *J. Geophys. Res.* **123,** 5886–5901, doi: 10.1029/2018JB015504.

Lior, I., A. Ziv, and R. Madariaga (2016). P-wave attenuation with implications for earthquake early warning, *Bull. Seismol. Soc. Am.* **106,** 13–22, doi: 10.1785/0120150087.

Ma, K., J. Mori, S. Lee, and S. Yu (2001). Spatial and temporal distribution of slip for the 1999 Chi-Chi, Taiwan, earthquake, *Bull. Seismol. Soc. Am.* **91,** 1069–1087, doi: 10.1785/0120000728.

Madariaga, R. (1976). Dynamics of an expanding circular fault, *Bull. Seismol. Soc. Am.* **65,** 163–182.

McGuire, R. K., and T. C. Hanks (1980). RMS accelerations and spectral amplitudes of strong ground motion during the San Fernando, California earthquake, *Bull. Seismol. Soc. Am.* **70,** 1907–1919.

Nof, R. N., and R. M. Allen (2016). Implementing the ElarmS earthquake early warning algorithm on the Israeli seismic network, *Bull. Seismol. Soc. Am.* **106,** 2332–2344, doi: 10.1785/0120160010.

Pittore, M., D. Bindi, J. Stankiewicz, A. Oth, M. Wieland, T. Boxberger, and S. Parolai (2014). Toward a loss-driven earthquake early warning and rapid response system for Kyrgyzstan (Central Asia), *Seismol. Res. Lett.* **85,** 1328–1340, doi: 10.1785/0220140106.

Ross, Z. E., and Y. Ben-Zion (2016). Toward reliable automated estimates of earthquake source properties from body wave spectra, *J. Geophys. Res.* **121,** 4390–4407, doi: 10.1002/2016JB013003.

Sato, T., and T. Hirasawa (1973). Body wave spectra from propagatingshear cracks, *J. Phys. Earth* **21,** 415–431.

Satriano, C., A. Lomax, and A. Zollo (2008). Real-time evolutionary earthquake location for seismic early warning, *Bull. Seismol. Soc. Am.* **98,** 1482–1494, doi: 10.1785/0120060159.

Savage, J. C. (1972). Relation of corner frequency to fault dimensions, *J. Geophys. Res.* **77,** 3788–3795.

Van Houtte, C., S. Drouet, and F. Cotton (2011). Analysis of the origins of κ (kappa) to compute hard rock to rock adjustment factors for GMPEs, *Bull. Seismol. Soc. Am.* **101,** 2926–2941, doi: 10.1785/0120100345.

Wang, G., X. Zhou, P. Zhang, and H. Igel (2002). Characteristics of amplitude and duration for near fault strong ground motion from the 1999 Chi-Chi, Taiwan Earthquake, *Soil Dynam. Earthq. Eng.* **22,** 73–96, doi: 10.1016/S0267-7261(01)00047-1.

Worden, C. B., M. C. Gerstenberger, D. A. Rhoades, and D. J. Wald (2012). Probabilistic relationships between ground-motion parameters and modified Mercalli intensity in California, *Bull. Seismol. Soc. Am.* **102,** no. 1, 204–221, doi: 10.1785/0120110156.

Wu, Y. M., and L. Zhao (2006). Magnitude estimation using the first three seconds P-wave amplitude in earthquake early warning, *Geophys. Res. Lett.* **33,** L16312, doi: 10.1029/2006GL026871.

Ziv, A., and I. Lior (2016). Real-time moment magnitude and stress drop with implications for real-time shaking prediction, *Bull. Seismol. Soc. Am.* **106,** 2459–2468, doi: 10.1785/0120160091.

Zollo, A., S. Colombelli, L. Elia, A. Emolo, G. Festa, G. Iannaccone, C. Martino, and P. Gasparini (2014). An integrated regional and onsite earthquake early warning system for southern Italy: Concepts, methodologies and performances, in *Early Warning for Geological Disasters: Scientific Methods and Current Practice*, F. Wenzel and J. Zschau (Editors), Springer-Verlag, Heidelberg, Berlin, Germany, doi: 10.1007/978-3-642-12233-0_7.

Manuscript received 3 June 2019
Published online 14 January 2020